The 27–28 October 1986 FIRE IFO Cirrus Case Study: In Situ Observations of Radiation and Dynamic Properties of a Cirrus Cloud Layer

WILLIAM L. SMITH, JR., PAUL F. HEIN AND STEPHEN K. COX

Department of Atmospheric Science, Colorado State University, Fort Collins, Colorado

(Manuscript received 3 February 1989, in final form 4 August 1989)

ABSTRACT

On 28 October 1986 the NCAR Sabreliner observed a cirrus cloud layer in the vicinity of Green Bay, Wisconsin. A portion of each flight leg was conducted over western Lake Michigan and over the adjacent western shore. The cirrus layer would be qualitatively described as optically thin and tenuous, yet broadband infrared effective emittances were found between about 0.4 and 0.6 while broadband shortwave extinction values ranged from as low as 5% to 32%. This investigation examines the bulk radiative properties of the cirrus layer and the horizontal variability of these radiative properties. In addition, the microphysical characteristics and the dynamic properties of the layer are presented and analyzed. The broadband infrared volume absorption coefficients were deduced for the cirrus layer and found to be very similar in terms of a dependence on temperature to results recently presented by other authors. Infrared radiative heating rates were calculated and found to be typical of the optically thin cirrus layer examined here. The horizontal structures of the radiative properties of the cirrus cloud layer and the vertical velocity observations were very similar. Both showed a smaller scale variation at the top of the cirrus layer which merged into larger scale common elements near the bases of the layer. Power spectra analyses of along-wind and cross-wind components near the base of the clouds sampled exhibited a steep spectral slope of k^{-3} at the smaller wave numbers (scalelengths greater than 1 km). This k^{-3} slope is characteristic of two-dimensional eddies. The same k^{-3} slope is present in the power spectra of the radiative properties. It is probable that these radiative properties, which are modulated by the cloud elements, have their scales determined by the eddies detected in the analysis of wind components.

1. Introduction

Cirrus clouds are recognized to be important modulators of the radiative energy distribution in the earth–atmosphere system and, thus, are important to weather and climate.

Recent advances in remote sensing by lidar and the availability of high altitude research aircraft have provided opportunities to study the radiative characteristics and microphysical composition of cirrus, in the hope that we may better understand these clouds which have been identified to be one of the major unsolved components in weather and climate research (Bretherton and Suomi 1973). Griffith et al. (1980) reported aircraft measurements of the radiative properties and microphysical composition of cirrus observed in the tropics during GATE, as did Paltridge and Platt (1981) for cirrus over New Mexico. Platt et al. (1987) reported the optical properties of midlatitude and tropical cirrus from a year's extensive LIRAD (developed by Platt 1973) observations. Platt and Harshvardhan (1988) used LIRAD results and the results of Heymsfield and Platt (1984) to investigate the sensitivity of climate to cirrus clouds. Several theoretical investigations of the infrared properties of cirrus clouds have been reported. Hunt (1973) and Liou (1974) conducted detailed investigations of the radiative properties of cirrus clouds in the atmospheric window region. Stephens (1980) presented 11 μm and broadband radiative transfer calculations through cirrus.

In this paper we present observations of cirrus cloud radiative, microphysical and dynamic properties, their variability and apparent scale sizes, as observed from the NCAR Sabreliner on 28 October 1986.

2. Flight and data description

The Sabreliner was flown near the western shore of Lake Michigan, close to Green Bay, Wisconsin, in what would be qualitatively described as a thin, tenuous cirrus layer. The Sabreliner sampled the cirrus at six altitudes through a thin cirrus deck with a banded structure. Cloud base was estimated to vary from heights of 9.0 to 9.4 km with cloud top estimated at 10.9 to 11.5 km. The videotape of the flight revealed an undercast of widely scattered altocumulus.

A racetrack pattern was flown with the flight legs oriented about 30 degrees off (to the right on the downwind legs) the mean wind direction (WNW). Although not visually obvious, it became apparent from

Corresponding author address: Mr. William L. Smith, Jr., Department of Atmospheric Science, Colorado State University, Fort Collins, CO 80523.

TABLE 1a. Cloud Sample 1 flight leg times, positions, and headings.

Height (km)	Start time (UTC)	Start Lat (deg N)	Start Long (deg W)	End time (UTC)	End Lat (deg N)	End Long (deg W)	Heading (deg)
11.4	1545:48	44.45	87.89	1548:58	44.29	87.41	120
10.2	1600:56	44.45	87.89	1604:31	44.27	87.36	119
9.0	1616:47	44.44	87.93	1620:41	44.28	87.36	113

TABLE 1b. Cloud Sample 2 flight leg times, positions, and headings.

Height (km)	Start time (UTC)	Start Lat (deg N)	Start Long (deg W)	End time (UTC)	End Lat (deg N)	End Long (deg W)	Heading (deg)
10.8	1553:20	44.54	87.39	1557:17	44.86	87.91	288
9.6	1607:45	44.45	87.21	1613:30	44.65	87.93	289
8.7	1624:44	44.48	87.36	1630:34	44.52	88.11	275

inspection of the data that the cloud sampled on the north side of the racetrack had different radiative and microphysical characteristics than the cloud sampled on the south side of the racetrack pattern, despite the fact that the two sides of the racetrack were only separated by a horizontal distance of 25 km. For this reason, the data from each racetrack side were treated separately. "Cloud Sample 1" on the south side of the racetrack pattern consisted of the flight legs at the 11.4, 10.2, and 9.0 km heights, while "Cloud Sample 2" on the north side of the racetrack pattern was sampled with flight legs at heights of 10.8, 9.6, and 8.7 km. Note that Cloud Sample 2 is geometrically thinner than Cloud Sample 1. Tables 1a and 1b list the times, position, and heading of the flight legs for each of the designated clouds. The vertical profiles of the mean downwelling shortwave (0.3–2.8 μm) and infrared (4–50 μm) irradiances in Fig. 1 and the mean ice water content (IWC) in Fig. 2 illustrate the differences between the two clouds.

The broadband fluxes were obtained from measurements made by pyranometers and pyrgeometers man-

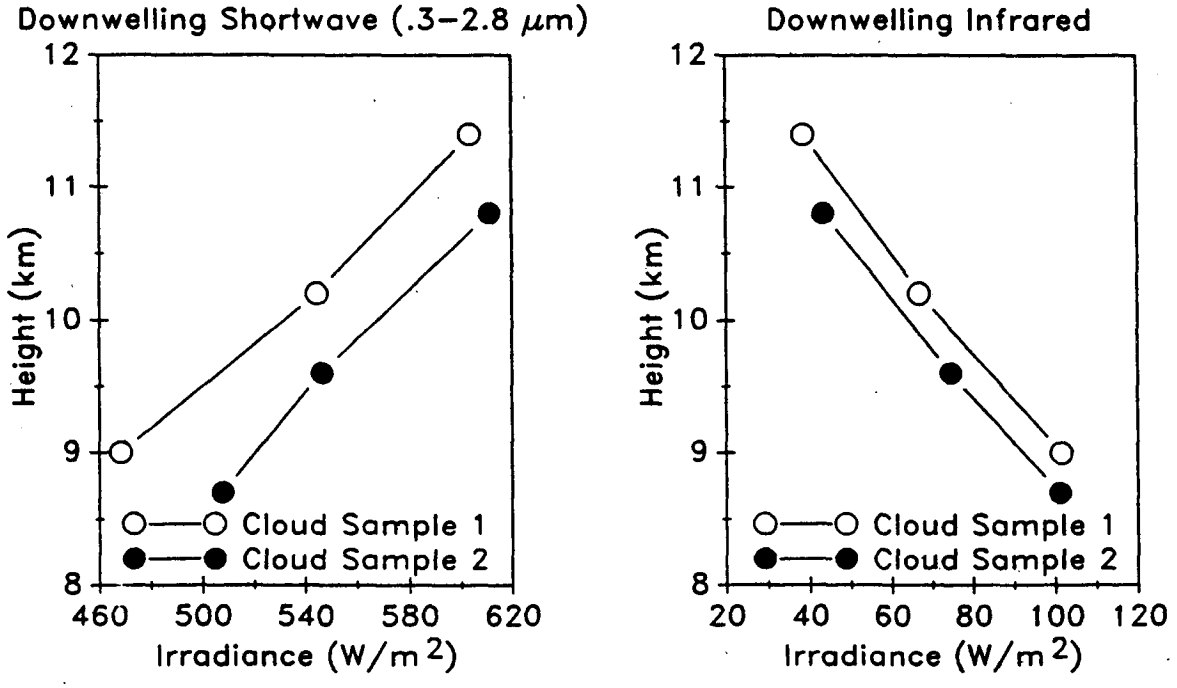

FIG. 1. Vertical profiles of mean downwelling shortwave and infrared irradiances.

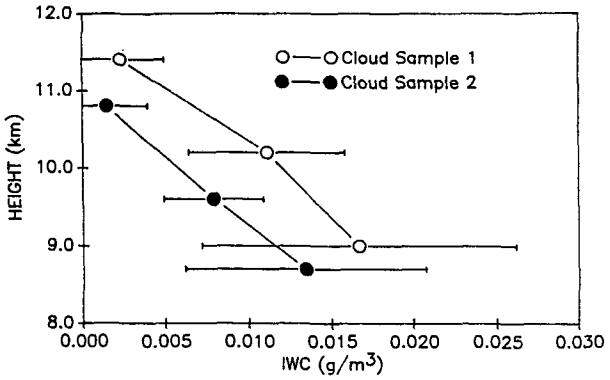

FIG. 2. Vertical profile of mean ice water content.

ufactured by Eppley Laboratories, Inc. For description of these radiometers and calibration procedures, see Albrecht and Cox (1976, 1977) and Smith, Jr. et al. (1988). In addition, the shortwave irradiances were corrected to a horizontal plane and normalized to common time by taking into account Sabreliner flight information (i.e., pitch, roll, and heading), as well as the sun–earth geometry (Rockwood and Cox 1976; Ackerman and Cox 1981). The microphysics data were obtained from the Particle Measuring System, Inc., (PMS) two-dimensional probes. These data are described by Heymsfield et al. (1990). For a description of the Sabreliner dataset, see Hein et al. (1987).

3. Broadband infrared radiative transfer model

a. Model discussion

In order to assess the impact of the cloud layers on infrared radiation, the broadband (4–50 μm) irradiance data were analyzed utilizing a broadband infrared radiative transfer model similar to that described by Cox and Griffith (1979). For clear sky, this model is capable of reproducing broadband divergence values which agree with observations (Albrecht et al. 1974). The integral emittance values of the three radiatively important gases, H_2O, CO_2, and O_3 were calculated from an integral transmission approximation which, in the absence of scattering, is given by

$$\epsilon(T, p_o, p)i = \frac{\int_{\lambda_1}^{\lambda_2} B(\lambda, T)[1 - \tau(\lambda, u[p_o, p], T)]d\lambda}{\int_0^{\infty} B(\lambda, T)d\lambda}, \quad (1)$$

where τ is the spectral transmittance for a layer bounded by the reference pressure p_o and pressure p containing the optical mass $u(p_o, p)_i$ of the appropriate optically active constituent. The index i represents the spectral band pass $\lambda_1 - \lambda_2$. $B(\lambda, T)$ is the Planck function where T represents temperature and λ represents wavelength. A list of the spectral bandpasses over which (1) was evaluated and the sources of the spectral transmissivity data are given in Cox and Griffith (1979).

Infrared irradiance values as a function of pressure were calculated from the infrared emittance values and atmospheric temperature and moisture profiles obtained from an average of two Green Bay radiosonde profiles on 28 October 1986 at 1400 and 1730 UTC. CO_2 was assumed to be uniformly mixed with a constant mixing ratio of 0.501 g kg^{-1}. The ozone mixing ratio profile and the moisture profile above the highest radiosonde observation were obtained by averaging the summer and winter midlatitude profiles from McClatchey et al. (1972). Due to instrument limitations, accurate absolute humidity measurements were not made at frost point temperatures less than −54°C. For this reason, our analysis was conducted for two assumed profiles of water vapor mixing ratio within the cloud layer (see Fig. 3). The first profile was constructed assuming that the entire cloud was saturated with respect to ice. The second profile was constructed using measurements from the frost point hygrometer at frost point temperatures (T_f) greater than −54°C and data from the Lyman-alpha absorption hygrometer at temperatures less than −54°C, since the frost point hygrometer fails to respond to humidity changes in this regime. Because no absolute calibration was available for the Lyman-alpha data, it was calibrated against the frost point hygrometer data at $T_f > -54$°C, and this curve was extrapolated to fit the Lyman alpha measurements at $T_f < -54$°C. The resulting profile (Fig. 3) may be more realistic than assuming ice saturation considering the tenuous nature of the cirrus cloud observed on this day.

With the exception of the treatment of cloud, the basic computational technique is identical to that of Griffith et al. (1980) where the irradiance at a pressure level p is given by (2). Here,

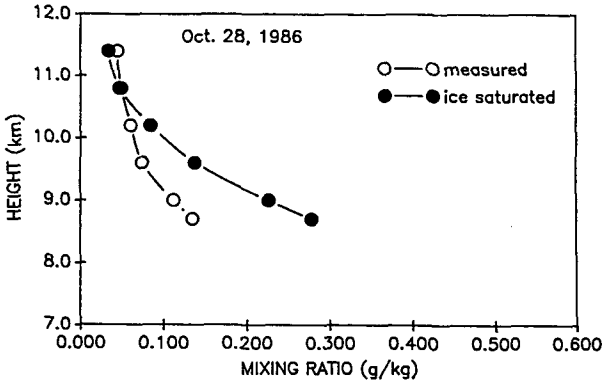

FIG. 3. The observed profile of water vapor mixing ratio and the ice saturation mixing ratio.

$$H(P_i) = \underbrace{\int_{P_o}^{P_i} B(T,p)\frac{\partial \epsilon_g}{\partial p}\,dp}_{A} + \underbrace{H_o\left[1 - \int_{P_o}^{P_i}\frac{\partial \epsilon_g}{\partial p}\,dp\right]}_{B} + \underbrace{\int_{P_o}^{P_i} B(T,p)\left(\frac{\partial \epsilon_{cld}}{\partial p} - \frac{\partial \epsilon_{ovl}}{\partial p}\right)dp}_{C} + \underbrace{H_o\left[1 - \int_{P_o}^{P_i}\left(\frac{\partial \epsilon_{cld}}{\partial p} - \frac{\partial \epsilon_{ovl}}{\partial p}\right)dp\right]}_{D}, \quad (2)$$

where

$$\frac{\partial \epsilon_{ovl}}{\partial p} = \frac{\partial(\epsilon_g \cdot \epsilon_{cld})}{\partial p}. \quad (3)$$

Here, ϵ_g is the sum of the integral flux emittances of the atmospheric gases minus a gaseous overlap correction in the column extending from the reference pressure level p_o (i.e., $p_o = 0$ for the downwelling calculation and $p_o = p_{sfc}$ for the upwelling calculation), to the pressure level p, ϵ_{ovl} is the grey cloud-gaseous overlap correction, $B(T, p)$ is the Planck function and H_o is the emitted irradiance at the reference pressure level [i.e., $H_o\,(p_o = 0) = 0$ and $H_o\,(p_o = p_{sfc}) = \sigma T_{sfc}^4$]. Thus, terms A and B on the right-hand side of (2) represent the energy emitted and transmitted, respectively, by the atmospheric gases while the terms C and D represent the energy emitted and transmitted, respectively, by the cloud aerosol (in this case, ice) minus the cloud-gaseous overlap correction given in (3). Because observations of the irradiance, temperature, and moisture profiles were made simultaneously on 28 October 1986 and assuming known concentrations of CO_2 and O_3, (2) may be solved for ϵ_{cld}.

We have chosen to treat the cloud as a greybody where:

$$\epsilon_{cld} = 1 - e^{-\tau_{cld}} \quad (4)$$

and

$$\tau_{cld} = \sum_i (K_i \cdot \overline{\mathrm{IWC}}_i \cdot \Delta Z_i) = \sum_i \sigma_i \cdot \Delta Z_i. \quad (5)$$

In (5), K_i is the greybody mass absorption coefficient; $\overline{\mathrm{IWC}}_i$ is the mean ice water content; σ_i is the broadband absorption coefficient (units m^{-1}), and ΔZ_i is the thickness for the ith cloud layer. Paltridge (1974) and Stephens (1978) have shown that when employing a constant value of K, (4) is a good descriptor of the radiative properties of water clouds. Griffith et al. (1980) successfully employed this relationship, assuming a constant value of K, to fit irradiance observations of cirrus obtained during GATE, although to date there is no theoretical basis supporting the assumption that the broadband cloud transmittance through cirrus is an exponential function of optical depth. Therefore, we have adopted (4), but with the assumption that K may be variable through the cirrus layer. This assumption is discussed in section 4.

b. Data analysis procedure

Because only one aircraft was used, measurements at different levels in the cloud were not made simultaneously. As a result, sampling errors may occur due to the nonsteady state of the cloud field and/or due to the possibility that the flight legs were not flown directly above or below each other. To minimize these errors and in an attempt to set some limits on the radiative properties observed on this day, the downwelling irradiance and IWC data for each flight leg were averaged in the following ways:

- Mean: Average using every measurement along the flight leg to determine a mean value for the cirrus cloud field.
- Thinner: Average the lowest 30% of the irradiance measurements and the lowest 30% of the IWC data to represent the optically thinner part of the cloud field.
- Thicker: Same as above but for the highest 30% to represent the optically thicker part of the cloud field.

The means and standard deviations of the data that constitute the profiles for the above cases are shown in Table 2.

For the downwelling irradiance calculation, Eqs. (1)–(5) were solved iteratively for the value of K that yields a calculated irradiance within ± 0.01 W m^{-2} of the observed irradiance at the cloud level in question. Because the variability in the upwelling irradiance observations was rather large due to the presence of lower level clouds, no attempt was made to incorporate these observations into the analysis. Instead, the K values retrieved from the downwelling calculation were used to calculate profiles of upwelling irradiance through the cirrus clouds. This enabled the computation of broadband, infrared heating rates (presented in section 4). We note that the calculated upwelling irradiances did lie within the range of observed values at the appropriate altitudes. The mean upwelling irradiance observed at cloud base was 252.5 (263.1) W m^{-2} for Cloud Sample 1 (Cloud Sample 2). Agreement at the cloud boundaries between the clear sky calculated irradiance and the mean observed irradiance was achieved by adjusting the background flux H_o of (2). For this flight, differences between the clear sky calculation and the mean pyrgeometer observation were about 13 W m^{-2} for the downwelling irradiance at cloud top and less than 10 W m^{-2} for the upwelling irradiance at cloud base. Besides the presence of scattered clouds outside of the cirrus boundaries, uncertainties in the specified temperature and gaseous profiles (particularly above the cirrus cloud top), as well

TABLE 2. The means (standard deviations) of the data that constitute the profiles for the mean, thinner, and thicker cloud cases. See Heymsfield et al. (1990) for a description of the microphysics data provided for this analysis.

Case	Z (km)	$H\downarrow$ (W m^{-2})	IWC (g m^{-3})	$\bar{D}_{mass}$ (cm)	Concentration (L^{-1})
			Cloud Sample 1		
A Mean	11.4	38.62 (1.31)	0.0002 (0.0002)	0.0083 (0.0010)	3.0928 (3.1914)
	10.2	66.83 (4.39)	0.0020 (0.0008)	0.0225 (0.0081)	4.4976 (2.9609)
	9.0	101.55 (5.56)	0.0047 (0.0032)	0.0423 (0.0179)	3.1835 (1.7476)
B Thinner	11.4	38.62 (0.18)	0.0 (0.0)	0.0083 (0.0006)	0.3833 (0.1274)
	10.2	61.34 (2.34)	0.0010 (0.0002)	0.0165 (0.0038)	3.6750 (1.5327)
	9.0	94.76 (3.27)	0.0013 (0.0005)	0.0213 (0.0027)	2.6262 (1.1165)
C Thicker	11.4	38.62 (0.99)	0.0004 (0.0002)	0.0078 (0.0005)	6.4250 (3.2786)
	10.2	71.56 (1.76)	0.0029 (0.0006)	0.0282 (0.0094)	4.9846 (4.4202)
	9.0	107.39 (2.61)	0.0089 (0.0012)	0.0568 (0.0108)	3.9286 (2.2835)
			Cloud Sample 2		
A Mean	10.8	43.42 (2.69)	0.0003 (0.0004)	0.0154 (0.0047)	1.2466 (1.6319)
	9.6	74.52 (4.03)	0.0024 (0.0009)	0.0364 (0.0071)	2.0171 (1.5023)
	8.7	101.08 (4.92)	0.0029 (0.0016)	0.0316 (0.0094)	4.3380 (2.8049)
B Thinner	10.8	43.42 (0.20)	0.0 (0.0)	0.0152 (0.0045)	0.2163 (0.2251)
	9.6	70.03 (1.17)	0.0015 (0.0003)	0.0339 (0.0067)	1.8205 (1.5857)
	8.7	96.47 (1.88)	0.0012 (0.0006)	0.0271 (0.0115)	3.4788 (2.6901)
C Thicker	10.8	43.42 (1.42)	0.0006 (0.0004)	0.0148 (0.0042)	2.9220 (1.8421)
	9.6	79.73 (1.46)	0.0034 (0.0007)	0.0374 (0.0052)	2.1595 (0.5978)
	8.7	107.47 (3.12)	0.0048 (0.0010)	0.0360 (0.0047)	5.1833 (1.3742)

as inaccuracies in the absolute measurement of irradiance all contribute to the differences noted above.

4. Results

The analysis of the cirrus layer data from 28 October 1986 was divided into two parts. First, the data were analyzed to infer a broadband, infrared-absorption coefficient to deduce the impact of the layer on infrared radiation. The relationship of this absorption coefficient to temperature and microphysical characteristics of the cloud are explored. Second, the horizontal variability of the cirrus layer is investigated. Radiation and atmospheric motion parameters are examined to deduce variability and horizontal scales of this variation.

a. Infrared properties

1) CLOUD EMITTANCES

The model deduced cloud emittances, i.e., the emittances due to the cloud aerosol, are shown in Fig. 4 as a function of ice–water path for Cloud Sample 1 and Cloud Sample 2. The results depict the tenuous nature of the cirrus observed on this day with emittance values approaching about 0.55 for Cloud Sample 1 and about 0.45 for Cloud Sample 2. The differences between the two cloud samples may be attributed to differences in optical thickness as Cloud Sample 2 has lower ice–water contents (see Fig. 2) and is geometrically thinner (see Tables 1a. and 1b.).

The emittances in Fig. 4 were retrieved for Cloud Sample 1 and Cloud Sample 2 with the observed water vapor mixing ratio profile. Assuming that the water vapor distribution in the cirrus layer was at ice saturation, produced cloud emittance values which were lower than those shown in Fig. 4 by less than 8%.

2) ABSORPTION COEFFICIENTS

Platt and Harshvardhan (1988), hereafter referred to as PH, discuss the relationship between cirrus cloud absorption and ice-water content and provide insight

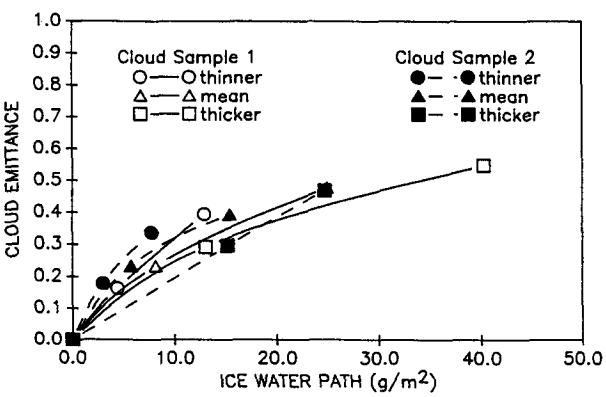

FIG. 4. Model deduced infrared emittance for Cloud Sample 1 and Cloud Sample 2 as a function of ice water path (IWP).

as to why the mass absorption coefficient, K, may not be a constant through a cirrus cloud of variable ice particle size distribution. As in PH, K may be considered as:

$$K = \frac{\sigma}{\text{IWC}} \approx \beta \frac{\bar{Q}_a}{r_e}, \tag{6}$$

where $\bar{Q}_a$ is the "effective absorption efficiency," r_e the "effective radius" for the size distribution, and β is a constant which includes the density of ice and an ice particle orientation factor. Theoretical computations of the absorption efficiency Q_a as a function of size parameter have been carried out by Herman (1962), Pinnick et al. (1979) and others. For incident energy in the infrared wavelengths, $\bar{Q}_a \approx cr_e$ (c is some constant) for size parameters typically found in stratiform water clouds and, thus, K is approximately constant. However, for ice clouds where typical ice crystal dimensions are known to be an order of magnitude larger than the water droplet dimensions found in stratiform clouds, the absorption efficiency approaches a value of unity so that K should vary inversely with r_e. This implies that K cannot be treated as a constant through cirrus unless r_e remains constant. This is clearly not the case for the clouds observed on 28 October 1986. Figure 5 shows the parameters $\bar{D}_{\text{mass}}$ and $D_{\max}$ varying as a function of height for Cloud Sample 1 and Cloud Sample 2. $\bar{D}_{\text{mass}}$ is the mean median mass-weighted ice particle dimension and $D_{\max}$ is the mean maximum-dimension measured across each flight leg (see Heymsfield et al. 1990 for a description of these parameters). Note that the inconsistency that appears in the radiative properties of the two cloud samples (see Fig. 1) and in the ice-water content (see Fig. 2) does not appear in the profile of these microphysical parameters. This is probably due to the fact that the concentration of ice particles measured in Cloud Sample 1 was nearly double that measured in Cloud Sample 2.

Figure 6 shows the retrieved K values for the mean cloud case as a function of $\bar{D}_{\text{mass}}$. As expected from the theoretical considerations above, the mass absorption coefficient varies inversely with particle size and ranges from about 0.046 to 0.023. Griffith et al. (1980) reported K values of 0.096, 0.080, and 0.076 for three cirrus clouds observed during a tropical eastern Atlantic experiment (GATE). The cirrus systems they sampled were anvils very close to deep convection. Paltridge and Platt (1981) deduced a K value of 0.056 to fit irradiance observations of cirrus cloud decks over New Mexico. The slopes of the lines connecting the points in Fig. 6 are considerably different for the two clouds sampled on 28 October. Understanding this difference is complicated by the fact that particles with diameters less than 37 μm were not resolved by the microphysics probes. Ackerman et al. (1990) showed, using high resolution spectral measurements in the 8–12 μm window, that most of the cirrus that they sampled were characterized by particle size distributions with effective radii less than 40 μm. We can only speculate that a population of smaller particles ($d < 37$ μm) and differences in the actual particle size distributions of Cloud Sample 1 and Cloud Sample 2 may account for the different slopes shown in Fig. 6. We note that while $\bar{D}_{\text{mass}}$ may not be the best parameter to represent the "effective" dimension of the cloud particle size distribution, it does support the interpretation of Eq. (6) that the mass absorption coefficients for cirrus clouds should vary inversely with ice particle dimension.

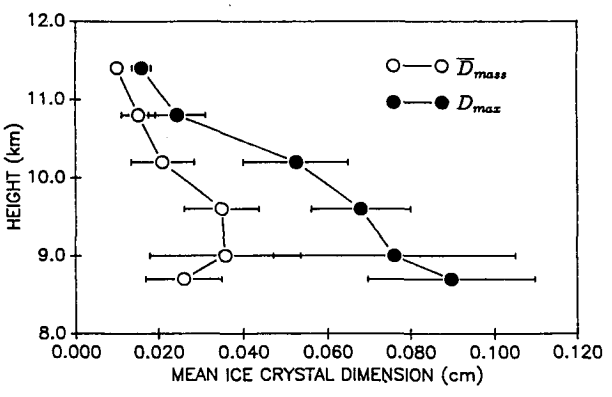

FIG. 5. Vertical profiles of the parameters $\bar{D}_{\text{mass}}$ and $D_{\max}$.

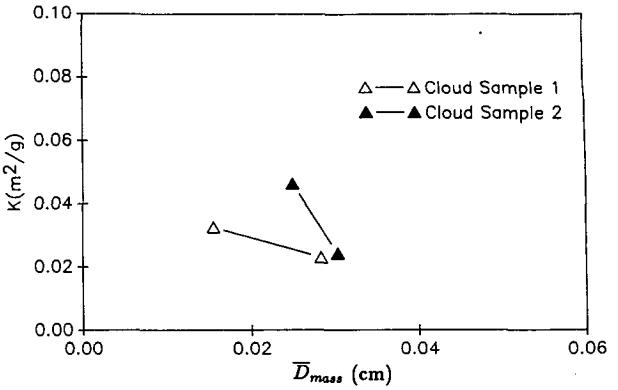

FIG. 6. Broadband mass absorption coefficients as a function of the parameter $\bar{D}_{\text{mass}}$.

Platt and Harshvardhan (1988) discuss the temperature dependence of cirrus infrared extinction based on data obtained by Platt et al. (1987) and Heymsfield and Platt (1984). The beam volume absorption coefficients (10–12 μm) deduced from these two independent datasets were found to be similar functions of temperature. We have computed broadband volume absorption coefficients (σ) where,

$$\sigma = K(\text{IWC}) \tag{7}$$

for Cloud Sample 1 and Cloud Sample 2, for the mean, thinner and thicker cases. Broadband volume absorption coefficient (σ) is plotted as a function of temperature in Fig. 7 against two regression lines for the data

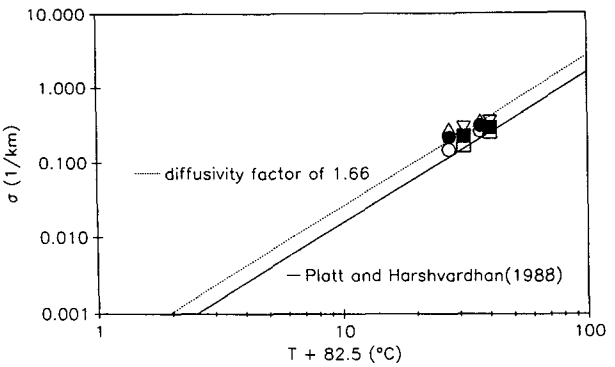

FIG. 7. Broadband volume absorption coefficients as a function of temperature.

in PH. The solid line fits the beam absorption coefficients as presented in PH while the dashed line fits these same values multiplied by a diffusivity factor of 1.66. The agreement between the dashed line and the σ values is very good, although several points lie closer to the solid line. Based on this limited sample of data, a diffusivity factor of 1.49 was determined to maximize this agreement.

3) HEATING RATES

The infrared heating rates shown in Table 3 indicate that Cloud Sample 1 and Cloud Sample 2 are influenced by radiative cooling (warming) in the upper (lower) layer. The magnitudes of these heating rates range systematically with ice-water path (IWP) from -0.35 (-0.41) to -1.17 (-0.76) °K day^{-1} in the upper layer of Cloud Sample 1 (Cloud Sample 2) and from 0.09 (-0.12) to 0.99 (0.63) °K day^{-1} in the lower layer of Cloud Sample 1 (Cloud Sample 2). As expected, the magnitudes of these heating rates are small when compared to heating rates deduced for optically denser cirrus cloud systems (e.g., Griffith et al. 1980; Ackerman et al. 1988). The mean IWP for the 2–3 km thick cirrus sampled on 28 October 1986 was about 20 g m^{-2}, nearly one-half the IWP found to extend 1.5 km below the tropical cirrus cloud tops studied by Griffith et al. (1980).

b. Horizontal variability

The horizontal variability and apparent scale sizes observed in the cirrus cloud layer on 28 October 1986 are characterized in terms of several radiation parameters, as well as atmospheric motion parameters, measured on board the NCAR Sabreliner.

We define the broadband infrared (4–50 μm) downward effective emittance ($\epsilon^* \downarrow$), the upward effective emittance ($\epsilon^* \uparrow$), the shortwave (0.3–2.8 μm) effective extinction (ζ), and the shortwave reflectance (ρ) by the following equations:

$$\epsilon^* \downarrow = \frac{H_B^{IR} \downarrow - \bar{H}_T^{IR} \downarrow}{\sigma \bar{T}_B^4 - \bar{H}_T^{IR} \downarrow}, \tag{8}$$

$$\epsilon^* \uparrow = \frac{H_T^{IR} \uparrow - \bar{H}_B^{IR} \uparrow}{\sigma \bar{T}_T^4 - \bar{H}_B^{IR} \uparrow}, \tag{9}$$

$$\zeta = \frac{\bar{H}_T^{SW} \downarrow - H_B^{SW} \downarrow}{\bar{H}_T^{SW} \downarrow}, \quad \text{and} \tag{10}$$

$$\rho = \frac{H_T^{SW} \uparrow - \bar{H}_B^{SW} \uparrow}{\bar{H}_T^{SW} \downarrow}. \tag{11}$$

For Cloud Sample 1 (Cloud Sample 2), $\bar{T}_T$ and $\bar{T}_B$ are the mean cloud top and base temperatures equal to 213.5 (216.9) K and 232.1 (234.4) K, respectively, $\bar{H}_T^{SW} \downarrow$ is the mean downwelling shortwave irradiance incident at cloud top equal to 604 (611) W m^{-2}, $\bar{H}_B^{SW} \uparrow$ is the mean upwelling shortwave irradiance at cloud base equal to 89.9 (84.6) W m^{-2}, $\bar{H}_T^{IR} \downarrow$ is the mean downwelling infrared irradiance at cloud top equal to 38 (43) W m^{-2} and $\bar{H}_B^{IR} \uparrow$ is the mean upwelling irradiance at cloud base equal to 252.5 (263.0) W m^{-2}. This makes $\epsilon^* \downarrow$ and ζ dependent only on the downwelling irradiance values ($H_B^{IR} \downarrow$, $H_B^{SW} \downarrow$) at cloud base and $\epsilon^* \uparrow$ and ρ dependent only on the upwelling irradiance values ($H_T^{IR} \uparrow$, $H_T^{SW} \uparrow$) at cloud top. We note that there may be a significant reflected component of the upwelling irradiance inherent in $\epsilon^* \downarrow$ and ζ.

1) RADIATIVE PROPERTIES

The histograms of infrared downward effective emittance ($\epsilon^* \downarrow$) in Fig. 8 and shortwave effective extinction (ζ) in Fig. 9 describe the variability in the radiative properties of the two cirrus samples. Despite the optically thin and tenuous appearance of this cirrus cloud layer, $\epsilon^* \downarrow$ is found to range from about 0.4 to 0.6, while ζ ranges from as low as 5% to 32%. Note also the differences between the two clouds with Cloud

TABLE 3. Broadband infrared heating rates (°K day^{-1}) for the mean, thinner, and thicker cloud cases.

z (km)	Thinner	Mean	Thicker
	Cloud Sample 1		
11.4			
‖	−0.34	−0.75	−1.17
10.2			
‖	0.09	0.53	0.99
9.0			
	Cloud Sample 2		
10.8			
‖	−0.41	−0.49	−0.76
9.6			
‖	−0.12	0.17	0.63
8.7			

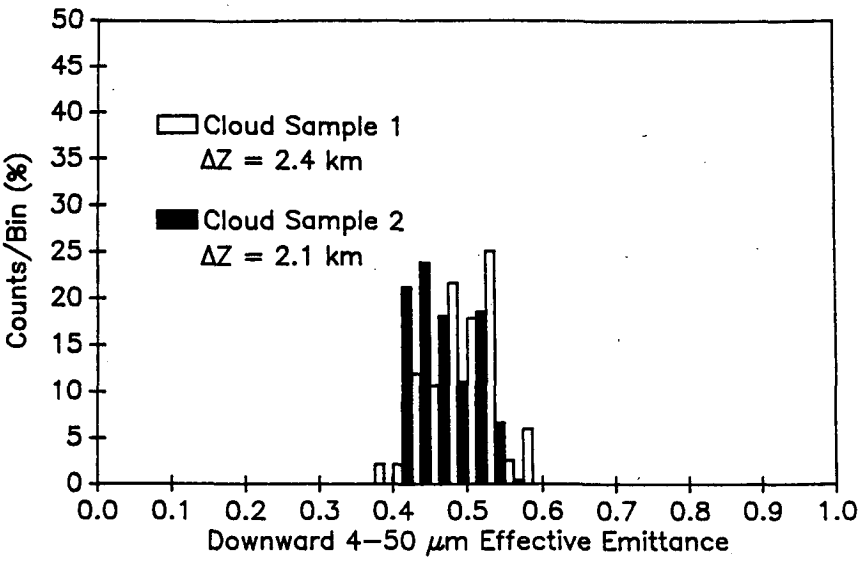

FIG. 8. Frequency distribution of infrared downward effective emittance.

Sample 1, on the average, having higher values of $\epsilon^* \downarrow$ and ζ than Cloud Sample 2. Cloud Sample 2 also has a wider range of values in ζ. The differences in these two radiative properties are due mainly to differences in the optical thickness of these two cloud samples, as Cloud Sample 1 was 0.3 km thicker and had larger ice water contents than Cloud Sample 2.

Here, $\epsilon^* \downarrow$ at cloud base is plotted as a function of ζ in Fig. 10. Although there is significant scatter about the regression lines of Cloud Sample 1 and Cloud Sample 2, both regression lines have nearly the same slope. The scatter may be due, in part, to the different regions of cloud affecting the pyranometer and pyrgeometer measurements (i.e., the slanted path taken by the direct component of the solar radiation versus the more isotropic infrared radiation). Possible explanations for the offset include the effects of cloud inhomogeneities and/or the possibility that the unmeasured cloud microphysical structure (i.e., small particles) was different in these two regions of the cirrus cloud layer.

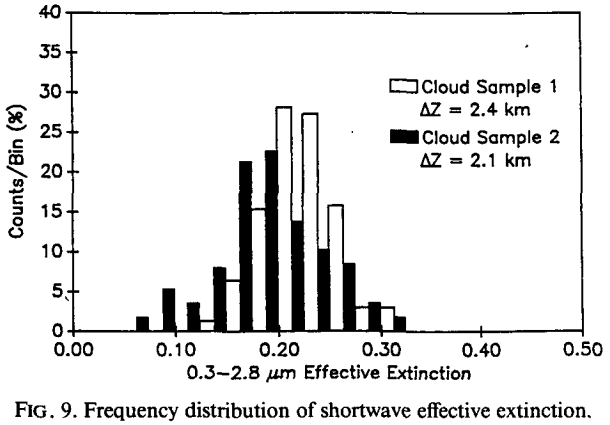

FIG. 9. Frequency distribution of shortwave effective extinction.

The infrared upward effective emittance ($\epsilon^* \uparrow$) is plotted as a function of the shortwave reflectance (ρ) in Fig. 11 for Cloud Sample 1 and Cloud Sample 2. The regression line fits the data of Cloud Sample 1 and shows good correlation between these two parameters in the thicker regions of both cloud samples. The thinner region of Cloud Sample 2 appears to be offset from the rest of the data again indicating the possible effects of cloud inhomogeneities and/or differences in cloud microphysics. It is interesting to note that the range in $\epsilon^* \uparrow(\rho)$ is almost identical to the range in $\epsilon^* \downarrow(\zeta)$.

2) SPATIAL SCALES

The spatial scales of the cloud features can be described by cumulative variance graphs. These graphs were created by first using a Fast Fourier Transform to create variance spectra. The variances were then summed in a cumulative fashion from the largest scalelengths (wavelengths) to the smallest. No detrending was done to the original data and no smoothing or averaging was done to the spectral points. Also, no points were removed due to the finite number of data points. This means that the first five to ten spectral points of the large scalelengths should only be considered to be qualitatively correct. The cumulative variance at smaller scalelengths should be correct because a more accurate representation of the variance at the larger scalelengths should only redistribute the energy among the larger scalelengths. Note that each scalelength (or wavelength) contains both a "peak" and a "valley". The following graphs of cumulative variance may be interpreted as showing the percentage of variance explained by scalelengths larger than the given scalelength.

The spatial scales of infrared downward effective emittance, the shortwave effective extinction, and

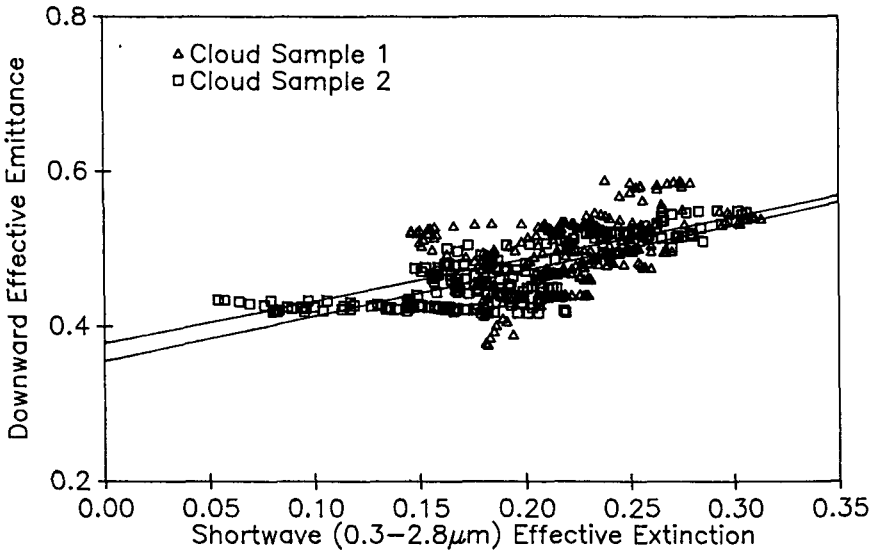

FIG. 10. Infrared downward effective emittance as a function of the shortwave effective extinction.

shortwave reflectance are described by the cumulative variance graphs of Figs. 12, 13 and 14. Most of the variance is found at the large scalelengths. For the infrared downward effective emittance and the shortwave reflectance, 90% of the variance is explained by scalelengths larger than 10 km. For the shortwave effective extinction, 90% of the variance is explained by scalelengths larger than 5 km. Thus, most of the variability of these clouds, as deduced from the Sabreliner radiometric measurements, is determined by the larger features. Different results were obtained for the shortwave effective extinction and reflectance because the variabilities in these parameters are defined by different streams (downwelling versus upwelling) of radiation in Eqs. (10) and (11). A higher percentage of the variance is found at the larger scalelengths in the infrared downward effective emittance than in the shortwave effective extinction. This is because the shortwave radiation, being highly anisotropic, is not smoothed as much by the hemispheric view of the radiometric instrumentation as is the infrared. The scales are better represented in the shortwave effective extinction graph. The similarity between the two shortwave effective extinction curves in Fig. 14 shows that the clouds have the same spacial scales even though Cloud Sample 2 is optically thinner than Cloud Sample 1.

Figure 15 displays the vertical velocity scalelengths at the different heights in Cloud Sample 2. Especially notable is the narrowing of scale with increasing height. Eighty percent of the variance is explained by features

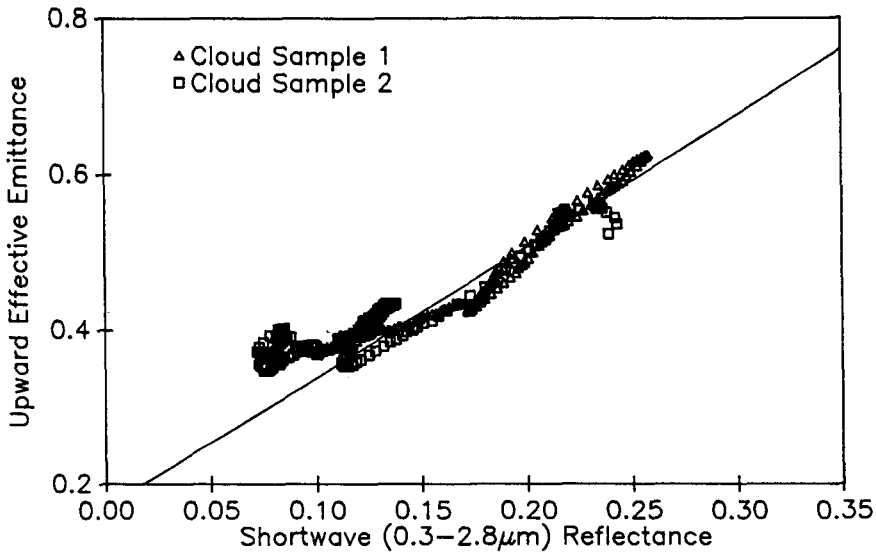

FIG. 11. Infrared upward effective emittance as a function of the shortwave reflectance.

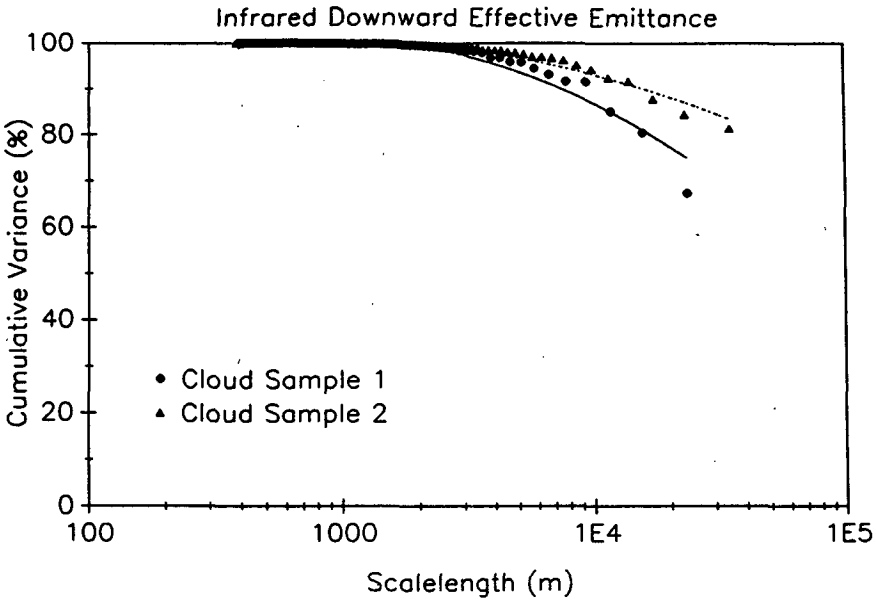

FIG. 12. Cumulative variance graph of infrared downward effective emittance.

larger than 4 km at the 10.7 km height, larger than 9 km at the 9.4 km height, and larger than 10 km at the 8.5 km height. This structure, showing smaller horizontal scales in upper layers of the cloud which then merge into larger scale features lower in the cloud has been observed in lidar data presented by Sassen et al. (1990). This may be indicating the presence of small convective cells in the upper part of the cloud with their larger precipitation trails beneath. (Note that these calculations were produced using vertical velocity deviations and therefore are not likely contaminated by the varying bias in the aircraft vertical velocity values.)

All of the cumulative variance graphs show this dominance of the larger scales to provide the majority of the variance.

The slope of the power spectra of the horizontal wind can be used to indicate the interaction between scales. Power spectra (smoothed with a six-point average and without the first five raw spectral points) of the along-wind and cross-wind components of the wind at the bottom of Cloud Sample 2 are shown in Fig. 16. Note the steep slope of k^{-3} at the smaller wavenumbers (scalelengths > 1 km). This suggests the transfer of eddy enstrophy (mean-squared vorticity) or the transfer

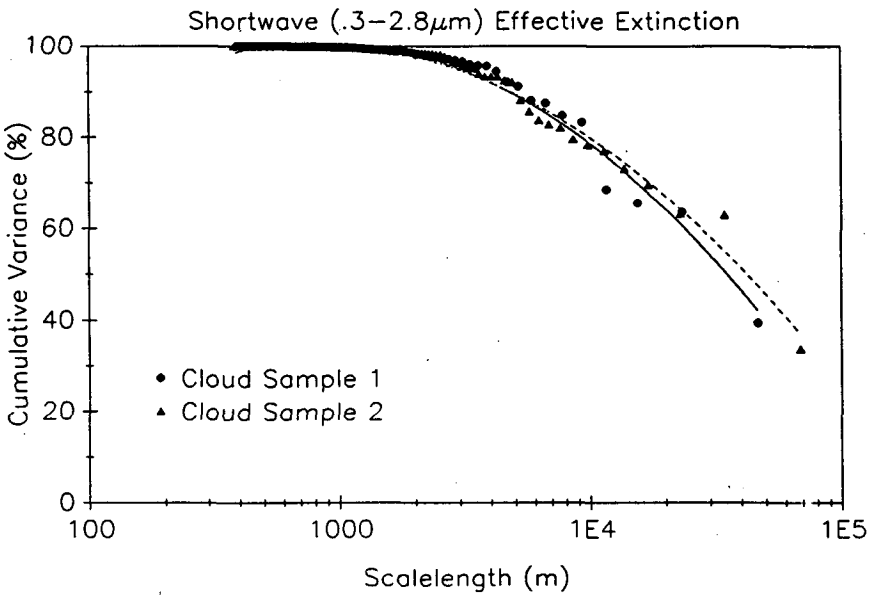

FIG. 13. Cumulative variance graph of shortwave effective extinction.

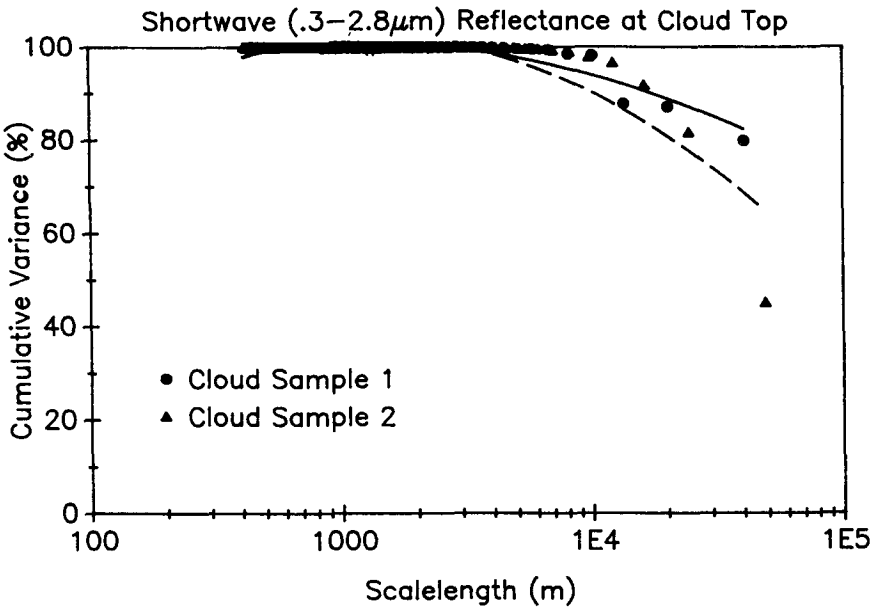

FIG. 14. Cumulative variance graph of shortwave reflectance at cloud top.

of quasi-geostrophic potential vorticity squared toward smaller scales according to two-dimensional turbulence theory. This cascade has been described by Gifford (1988), Charney (1971), and Kraichnan (1967), and is a result of the eddies being effectively two-dimensional. The scales are too small for Charney's geostrophic turbulence (with its quasi-geostrophic potential vorticity), however, the close proximity of the tropopause and the strong temperature inversion is likely constraining the eddies into an effectively two-dimensional flow with an enstrophy cascade. The layer is very stable with a strong temperature inversion and a weak wind shear. The layer has a Richardson number of 19.2. The Richardson number is proportional to the ratio of the buoyancy force suppression of turbulent energy to the production of turbulent energy by the wind shear. Values of the Richardson number greater than zero are considered stable.

The same slope is apparent in the power spectra of the downwelling shortwave and infrared irradiance

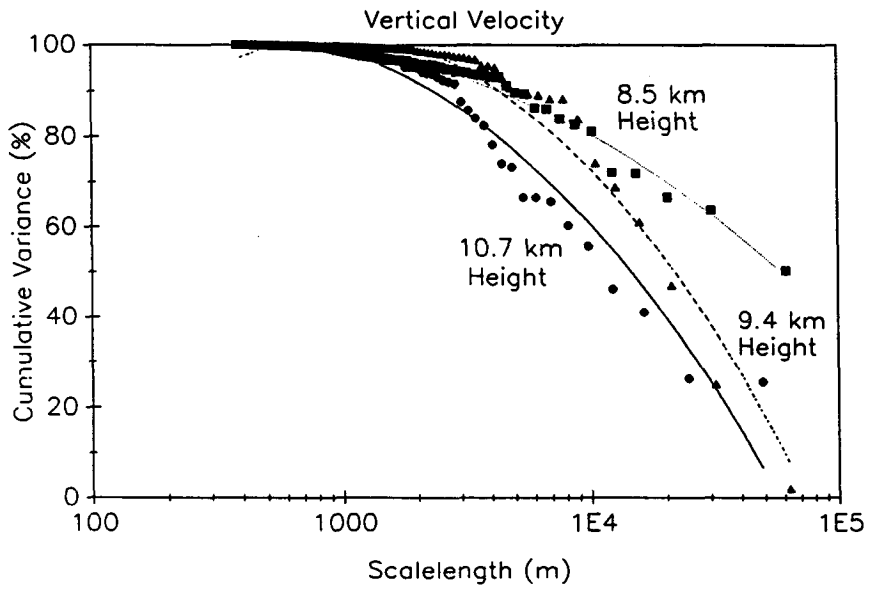

FIG. 15. Cumulative variance graph of vertical velocity at different heights in Cloud Sample 2.

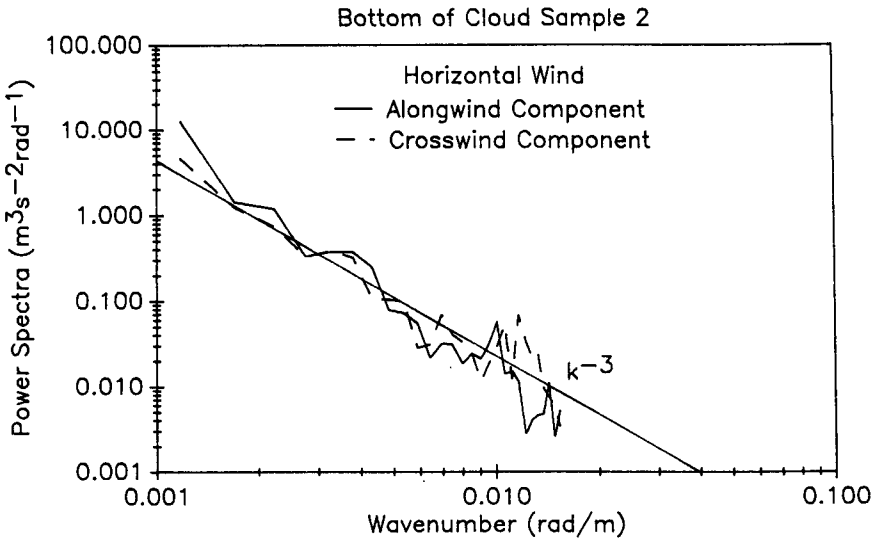

FIG. 16. Power spectra of the along-wind and cross-wind components of the horizontal wind at cloud base of Cloud Sample 2.

shown in Fig. 17. It is probable that the downwelling irradiances, modulated by the cloud elements, have their scales determined by the eddies of the wind. The same slope at the smaller wavenumbers was also found in the Cloud Sample 1 data.

5. Conclusions

Observations of the radiative, microphysical, and dynamic properties of cirrus clouds observed from the NCAR Sabreliner on 28 October 1986 have been presented. Broadband mass-absorption coefficients were deduced as a function of depth into the cirrus cloud and found to vary with particle dimension. These values were similar to those deduced by other authors. Broadband volume absorption coefficients were deduced and found to exhibit a similar dependence on temperature as the data presented in Platt and Harshvardhan (1988). This agreement was maximized when employing a diffusivity factor of 1.49. Calculated infrared heating rates were typical of thin cirrus layers with the cloud top cooling and cloud base warming becoming more accentuated for the denser portions of cloud. The broadband emittances due to the cloud aerosol were found to approach 0.5 to 0.6, in spite of the tenuous appearance of the cloud layer and the shortwave extinction values ranging from .05 to .32. The cirrus clouds were observed to exhibit significant horizontal variability. A significant amount of scatter was evident when attempting to relate the broadband

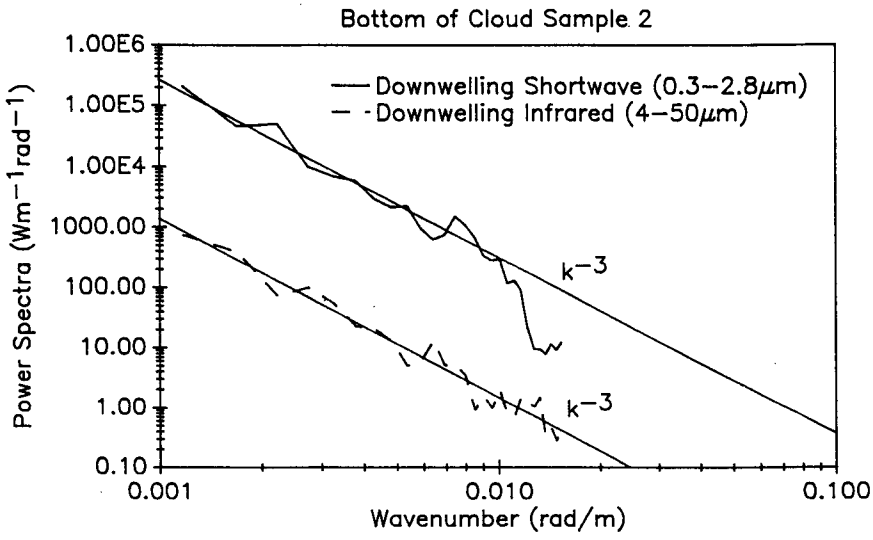

FIG. 17. Power spectra of the downwelling shortwave and infrared irradiances at cloud base of Cloud Sample 2.

infrared and shortwave radiative properties ($\epsilon^* \downarrow$ and ζ), most likely due to cloud inhomogeneities. Much better correlation was found between $\epsilon^* \uparrow$ and ρ. Most of the variance was explained at the larger scalelengths ($\sim$10 km). The apparent scale size in the vertical velocity measurements was found to narrow with increasing altitude suggesting that the dominant scale sizes decrease with increasing altitude. Finally, the steep spectra slope of k^{-3} is found to be similar for the u and v components of the wind and the downwelling irradiance suggesting that the scales of variability in the downwelling irradiance may be determined by eddies imposed on the larger scale wind field. These observations should serve as part of a growing database to which future cirrus cloud modeling efforts can be compared.

Acknowledgments. We are grateful to Dr. Andrew Heymsfield and Karen Miller for providing the reduced microphysics data. We also thank NCAR's Research Aviation facility for acquisition of the Sabreliner data and NCAR's Scientific Computing Division (SCD) for their computer support. NCAR is sponsored by the National Science Foundation. Special thanks are extended to Ms. Melissa Tucker for preparation of this manuscript. This research has been supported by the National Science Foundation under Grant ATM-8521214 and National Aeronautics and Space Administration Grant NAG 1-554.

REFERENCES

Ackerman, S. A., and S. K. Cox, 1981: Aircraft observations of the shortwave fractional absorptance of nonhomogeneous clouds. *J. Appl. Meteor.*, **20,** 128–133.

——, W. L. Smith, J. Spinhirne and H. E. Revercomb, 1990: The 27–28 October 1986 FIRE cirrus case study: spectral properties of cirrus clouds in the 8–12 μm window. *Mon. Wea. Rev.*, **118,** 2377–2388.

——, K. N. Liou, F. P. J. Valero and L. Pfister, 1988: Heating rates in tropical anvils. *J. Atmos. Sci.*, **45,** 1606–1623.

Albrecht, B., and S. K. Cox, 1976: Radiation data reduction procedures for Sabreliner, C-10 and DC-6 aircraft during GARP Atlantic Tropical Experiment. Atmos. Sci. Pap. No. 244, Colorado State University, Ft. Collins, 100 pp. [Available from the Department of Atmospheric Science, Colorado State University, Fort Collins, CO 80523.]

——, and ——, 1977: Procedures for improving pyrgeometer performance. *J. Appl. Meteor.*, **16,** 188–197.

——, M. Poellot and S. K. Cox, 1974: Pyrgeometer measurements from aircraft. *Rev. Sci. Instrum.*, **45,** 33–38.

Bretherton, F. P., and V. E. Suomi, 1983: First international satellite cloud climatology project regional experiment (FIRE) Research Plan, 76 pp. [Available from the National Climatic Program Office, Rm. 108, 11400 Rockville Pike, Rockville, MD., 20852.]

Charney, J., 1971: Geostrophic turbulence. *J. Atmos. Sci.*, **28,** 1087–1095.

Cox, S. K., and K. T. Griffith, 1979: Estimates of radiative divergence during phase III of the GARP Atlantic tropical experiment: Part I. methodology. *J. Atmos. Sci.*, **36,** 575–585.

Gifford, F. A., 1988: A similarity theory of tropospheric turbulence energy spectrum. *J. Atmos. Sci.*, **45,** 1370–1379.

Griffith, K., S. K. Cox and R. G. Knollenberg, 1980: Infrared radiative properties of tropical cirrus clouds inferred from aircraft measurements. *J. Atmos. Sci.*, **37,** 1077–1087.

Hein, P. F., S. K. Cox and C. M. Johnson-Pasqua, 1987: The Sabreliner dataset of the FIRE Cirrus IFO: FIRE Series No. 1. Atmos. Sci. Pap. No. 418, Colorado State University, Ft. Collins, 52 pp. [Available from the Department of Atmospheric Science, Colorado State University, Fort Collins, CO 80523.]

Herman, B. M., 1962: Infrared absorption, scattering, and total attenuation cross sections for water spheres. *Quart. J. Roy. Meteor. Soc.*, **88,** 143–150.

Heymsfield, A. J., and C. M. R. Platt, 1984: A parameterization of the particle size spectrum of ice clouds in terms of the ambient temperature and the ice water content. *J. Atmos. Sci.*, **41,** 846.

——, K. M. Miller and J. Spinhirne, 1990: The 27–28 October 1986 FIRE IFO cirrus case study: Cloud structure and composition from in situ measurements. *Mon. Wea. Rev.*, **118,** 2313–2329.

Hunt, G. E., 1973: Radiative properties of terrestrial clouds at visible and infrared thermal window wavelengths. *Quart. J. Roy. Meteor. Soc.*, **99,** 346–369.

Kraichnan, R. H., 1967: Inertial ranges in two-dimensional turbulence. *Phys. Fluids,* **10,** 1417–1423.

Liou, K.-N., 1974: On the radiative properties of cirrus in the window region and their influence on remote sensing of the atmosphere. *J. Atmos. Sci.*, **31,** 522–532.

——, 1986: Review: influence of cirrus clouds on weather and climate processes: a global perspective. *Mon. Wea. Rev.*, **114,** 1167–1197.

McClatchey, R., R. A. Fenn, J. E. A. Selby, F. E. Volz and J. S. Garing, 1972: Optical properties of the atmosphere, 3rd ed. AFCRL-72-0497, Air Force Cambridge Research Labs., 107 pp.

Paltridge, G. W., 1974: Infrared emissivity, shortwave albedo, and the microphysics of stratiform water clouds. *J. Geophys. Res.*, **79,** 4053–4058.

——, and C. M. R. Platt, 1981: Aircraft measurements of solar and infrared radiation and the microphysics of cirrus clouds. *Quart. J. Roy. Meteor. Soc.*, **107,** 367–380.

Pinnick, R. G., S. G. Jennings, P. Chylek and H. J. Auverman, 1979: Verification of a linear relation between IR extinction, absorption, and liquid water content of fogs. *J. Atmos. Sci.*, **36,** 1577–1586.

Platt, C. M. R., 1973: Lidar and radiometric observations of cirrus clouds. *J. Atmos. Sci.*, **30,** 1191–1294.

—— and Harshvardhan, 1988: Temperature dependence of cirrus extinction: implications for climate feedback. *J. Geophys. Res.*, **93,** 11 051–11 058.

——, J. C. Scott and A. C. Dilley, 1987: Remote sounding of high clouds. VI: Optical properties of midlatitude and tropical cirrus. *J. Atmos. Sci.*, **44,** 729–747.

Rockwood, A. A., and S. K. Cox, 1976: Satellite inferred albedo over northwestern Africa. Atmos. Sci. Pap. No. 262, Colorado State University, Ft. Collins, 64 pp. [Available from the Department of Atmospheric Science, Colorado State University, Fort Collins, CO 80523.]

Sassen, K., C. J. Grund, J. Spinhirne, M. Hardesty and J. M. Alvarez, 1990: The 27–28 October 1986 FIRE IFO Cirrus Case Study: A five lidar view of cirrus cloud structure and evaluation. *Mon. Wea. Rev.*, **118,** 2288–2312.

Smith, Jr., W. L., S. K. Cox and V. Glover, 1988: Temperature sensitivity of Eppley broadband radiometers. Atmos. Sci. Pap. No. 423, Colorado State University, Ft. Collins, 12 pp. [Available from the Department of Atmospheric Science, Colorado State University, Fort Collins, CO 80523.]

Stephens, G. L., 1978: Radiation profiles in extended water clouds, II: parameterization schemes. *J. Atmos. Sci.*, **35,** 2123–2132.

——, 1980: Radiative properties of cirrus clouds in the infrared region. *J. Atmos. Sci.*, **37,** 435–446.